Nanoscale

PAPER

View Article Online
View Journal

Cite this: DOI: 10.1039/d5nr05458c

Co-designing growth factors for the synthesis of (6, 5)-enriched single-walled carbon nanotube horizontal arrays

Junxiao Li,†[a] Sizhe Lin,†[a] Wei Liu,[a] Changlong Li,[b] Jiacheng Song,[b] Zhiwei Liu,[b] Yue Hu [b] and Shuchen Zhang *[a]

Received 26th December 2025,
Accepted 23rd March 2026

DOI: 10.1039/d5nr05458c

rsc.li/nanoscale

Precise control over the diameter and chirality of single-walled carbon nanotubes (SWNTs) is critical for scalable electronic applications, yet it remains a challenge for horizontally aligned arrays. Although low-temperature powder synthesis routinely yields sub-1 nm SWNTs with relatively high chirality selectivity, directly transferring these growth conditions to substrate-guided horizontal arrays has been hindered by poorly understood catalyst evolution and coupled growth factors (gas, temperature, pressure *etc*). Here, we employ a machine-learning-assisted framework that integrates systematic experiments with interpretable models to optimize the growth parameters, enabling sub-1 nm SWNT growth in horizontal arrays at low temperatures. Our ML model reveals that SWNT formation is governed by kinetic competition between amorphous-carbon deposition and graphitized-carbon incorporation, with catalytic cracking acting as the dominant carbon source under low-temperature conditions. Further, we successfully achieve horizontally aligned SWNT arrays enriched in (6, 5) nanotubes with a chiral selectivity of approximately 70% at 650 °C under an optimized environment predicted by the ML model. This is the first demonstration of sub-1 nm chiral-selective growth in horizontal arrays at such a low temperature. This work bridges the long-standing gap between powder and horizontal-array growth and establishes a rational, data-driven strategy for the deterministic synthesis of SWNTs.

1. Introduction

Single-walled carbon nanotubes (SWNTs) exhibit highly structure-dependent optical, electronic, and mechanical properties, making precise control over their diameter and chirality a central yet long-standing objective in nanomaterials research.[1–5] Achieving deterministic synthesis remains challenging because catalyst stability is affected by structure and composition, carbon feedstock chemistry and the local growth environment, which interact in complex and often nonintuitive ways.[6–11]

The prevailing understanding attributes the resulting chirality distribution of SWNTs to nucleation thermodynamics, growth kinetics, and the size and crystal structure of catalyst nanoparticles.[12–17] Several catalyst-engineering strategies have successfully demonstrated the selective enrichment of specific chiralities. For example, Yang *et al.* employed W_6Co_7 catalysts exposing the (0012) facet to produce (12, 6) tubes, whereas Zhang *et al.* introduced a symmetry-matching design principle that enabled the growth of (12, 6) and (8, 4) tubes using Mo_2C and WC catalysts, respectively.[18–20] Nonetheless, most selectively synthesized chiralities remain metallic ($2n$, n) tubes, reflecting the kinetic dominance intrinsic to high-temperature growth conditions, under which only a narrow subset of catalyst species retain structurally stable configurations, thereby suppressing thermodynamically governed assembly pathways due to the limited availability of carbon atoms.

In contrast, low-temperature growth of SWNTs provides a broader design window for chirality control because a wider range of catalyst compositions can maintain stable and well-defined structures.[21] Consistent with this rationality, powder samples from chemical vapor deposition (CVD) have long yielded enriched chiralities such as (6, 5),[22–25] (7, 5),[26–28] (7, 6),[29] and (9, 8),[30] which are more inclined towards selection by interface thermodynamic between SWNT and catalysts. However, a persistent discrepancy arises when these powder-based strategies are directly applied to the growth of horizontally aligned SWNT arrays on single-crystal substrates. While powder SWNT samples readily produce sub-1 nm nanotubes, substrate-guided horizontal-array growth—essential for wafer-scale device integration—typically results in substantially larger diameters.[31] This inconsistency con-

[a]State Key Laboratory of Precision and Intelligent Chemistry, Department of Materials Science and Engineering, School of Chemistry and Materials Science, University of Science and Technology of China, Hefei, Anhui 230026, China. E-mail: zhangshuchen@ustc.edu.cn
[b]Key Laboratory of Carbon Materials of Zhejiang Province, College of Chemistry and Materials Engineering, Wenzhou University, Wenzhou 325000, P. R. China
†These authors contributed equally to this work.

strains the accessible chiral structure of SWNTs in aligned arrays and obscures the fundamental mechanisms governing catalyst evolution and nanotube nucleation. Resolving this long-standing contradiction requires identifying the true rate-limiting and structure-determining factors in the SWNT growth—a challenge made more difficult by the strong correlations among synthesis variables, many of which cannot be independently tuned through experiments alone.

Recently, machine learning (ML) has presented a powerful route for extracting mechanistic insights from complex and multidimensional synthesis datasets.[32,33] By identifying hidden interactions among growth parameters, ML has begun to reshape approaches for catalyst discovery and mechanism elucidation.[34] Notably, Zhang *et al.* developed the CARCO platform, which carried out millions of simulated experiments over 43 days and identified a high-performance Ti–Pt catalyst for dense horizontal-array growth with an experimental prediction accuracy of 56.25%.[35] These achievements highlight the transformative potential of data-driven strategies in revealing previously inaccessible governing principles, implying the possibility of addressing the aforementioned issue.

Herein, we establish an ML-assisted framework that integrates systematic experimental datasets with interpretable models to identify the parameters that enable sub-1 nm SWNT growth in horizontal arrays at low temperatures. Our ML model shows that, under low-temperature conditions, SWNT formation is governed by the competition between amorphous-carbon deposition and graphitized-carbon incorporation, with catalytic cracking of carbon sources serving as the dominant carbon supply pathway relative to thermal decomposition. Regulating the carbon-atom flux shifts carbon nanotube formation from kinetically dominated accumulation toward thermodynamically guided assembly, thereby favoring the nucleation of structurally stable SWNT species. Further, we achieved horizontally aligned SWNT arrays enriched in the chiral (6, 5) tubes with a selectivity of 70% at 650 °C for the first time using the best optimized growth factors on catalysts and environment predicted by the ML model. This mechanistic understanding, coupled with data-driven guidance, reconciles the longstanding disparity between powder and horizontal-array growth and establishes a rational pathway toward the controlled synthesis of structurally well-defined SWNT arrays.

2. Methods

Preparation of catalysts on quartz substrate

0.1164 g of $Co(NO_3)_2{\cdot}6H_2O$ and varying amounts of $(NH_4)_6Mo_7O_{24}{\cdot}4H_2O$ were dissolved in 80 mL of deionized water under ultrasonic treatment for 10 min. The mass of $(NH_4)_6Mo_7O_{24}{\cdot}4H_2O$ was adjusted to 0 g, 0.0241 g, 0.0354 g, 0.0708 g and 0.0708 g, with the final condition prepared in the absence of $Co(NO_3)_2{\cdot}6H_2O$, corresponding to Co/Mo ratios of 1 : 0, 3 : 1, 2 : 1, 1 : 1 and 0 : 1, respectively. The resulting precursor solutions were subsequently diluted 100-fold with ethanol, yielding a final Co^{2+} concentration of 0.05 mmol L^{-1}.

Single-crystal ST-cut quartz substrates (single side polished, miscut angle <0.5°, surface roughness <5 Å; purchased from Hefei Kejing Materials Technology Co., Ltd, China) were sequentially ultrasonically cleaned in deionized water, acetone, ethanol and deionized water, each for 15 min. After cleaning, the quartz substrates were annealed in air at 900 °C for 8 h.

For catalyst deposition, 5 μL of the precursor solution was drop-cast onto each quartz substrate. The quartz substrates were then heated in a muffle furnace at 450 °C for 60 min with a ramping rate of 5 °C min^{-1} to ensure complete oxidization and dispersion of the catalyst precursors.

Growth of single-walled carbon nanotubes

The quartz substrate was placed in a 1-inch quartz tube and heated to 500 °C over 30 min under an Ar flow of 200 sccm. Upon reaching 500 °C, H_2 was introduced at a flow rate of 100 sccm and maintained for 30 min to reduce the catalyst. After the reduction step, the H_2 flow was terminated, and the system was further heated to the designated growth temperature. The Ar flow rate was then adjusted to a specified value (50, 100, 150, and 200 sccm), and CO was introduced at 50 sccm to initiate SWNT growth for 30 min. After SWNT growth, the CO flow was stopped, and the system was cooled to room temperature under 200 sccm Ar.

When ethanol was employed as the carbon source, the procedure was modified as follows. After catalyst reduction, the system was heated to the target temperature under an Ar/H_2 atmosphere and held for extra 5 min. The flow rates of Ar and H_2 were then each fixed at 200 sccm. Ethanol vapor was introduced by passing an independent Ar stream through an ethanol bubbler at a flow rate of 20, 40, 60, 100, or 150 sccm, and SWNT growth was carried out for 30 min. Following SWNT growth, the ethanol supply was terminated, and the system was cooled to 500 °C under an Ar/H_2 atmosphere. The H_2 flow was subsequently stopped, and the furnace was cooled to room temperature under a pure Ar flow.

Bayesian regression model training and validation

Three Bayesian regression models were performed on R 4.5.1, and the R code script was run on RStudio 2024.12.1, under a Windows 10 × 64 system.

Fitting of growth ability (CO as carbon source), run by Bayesian logistic regression model: Markov chains = 4, cores = 4, iteration = 8000, warmup = 6000, adapt_delta = 0.95, max_treedepth = 15 for running the model.

Fitting of growth ability (ethanol as carbon source), run by Bayesian logistic regression model: Markov chains = 4, cores = 4, iteration = 8000, warmup = 6000, adapt_delta = 0.95, max_treedepth = 15 for running the model.

Fitting of small-diameter selectivity, run by Bayesian nonlinear regression model: Markov chains = 4, cores = 4, iteration = 6000, warmup = 3000, adapt_delta = 0.98, max_treedepth = 15.

The validation process was performed with the BRMS package built-in diagnostic during the posterior analysis of the models. The BRMS package checks detailed posterior distribution information for model parameters, with validation of

the stationary and convergent distributed Markov chain and sufficient number of posterior samples.

Characterization

The morphology of SWNTs was characterized by SEM (FEI Apreo, operated at 2 kV) and AFM (Park XE7, non-contact mode). The chirality of SWNT arrays was determined by Raman spectroscopy (Renishaw inVia Reflex) using excitation wavelengths of 532 and 633 nm, complemented by UV-Vis-NIR (Shimadzu, UV-3600 spectrometer). TEM (JEOL JEM-2100F, operated at 200 kV) was employed to examine the reduced catalyst nanoparticles.

In addition, the specific content of chiral SWNTs was evaluated by UV-Vis-NIR spectroscopy. For this purpose, an aqueous sodium dodecyl sulfate (SDS, 1 wt%) solution was employed as the dispersion medium. The SWNTs were transferred from 80 quartz substrates into the SDS solution and subsequently dispersed by ultrasonication for 2 h. To ensure accurate background correction, a reference solution was prepared by subjecting an identical number of blank quartz substrates to the same treatment in an SDS solution of the same concentration under identical conditions. The resulting background signal was subtracted from the measured spectra, thereby isolating the intrinsic optical response of the SWNTs for subsequent analysis.

3. Results and discussion

The controllable synthesis of SWNTs critically depends on understanding the complex interplay among growth parameters that jointly govern nucleation, elongation, and the resulting chiral structure. Despite decades of intensive investigation, a predictive understanding of SWNT growth remains elusive, largely owing to the highly nonlinear, strongly coupled, and often non-monotonic nature of the governing parameters. As a result, conventional trial-and-error experimental approaches are inefficient and insufficient for resolving such complexity. To address this challenge, we employed an ML approach trained on experimentally derived data to capture the multifactorial interactions intrinsic to the chirality-selective growth of SWNTs (Fig. 1). By learning internal correlations among growth variables, the ML model enables the identification of low-temperature growth conditions and optimized parameter combinations that are difficult to directly access using traditional experimental strategies.

Given their widespread use in powder synthesis and horizontally aligned SWNT growth, cobalt-based catalysts were selected as representative systems, including pure Co and Co–Mo alloy catalysts. Initial exploration experiments were conducted using Co catalysts with carbon monoxide (CO) as the carbon source. As shown in Fig. 2a–d, no SWNT growth was observed at 800 °C under a fixed CO concentration. Reducing the temperature to the range of 750–650 °C resulted in pronounced nanotube growth, whereas further cooling to 600 °C again strongly suppressed growth. These observations clearly indicate that low-temperature SWNT growth cannot be rationalized by temperature alone. Instead, the growth behavior emerges from the coupled effects of temperature, carbon-source partial pressure, and catalyst composition. Consequently, identifying growth windows that explicitly capture these interdependencies is essential for understanding

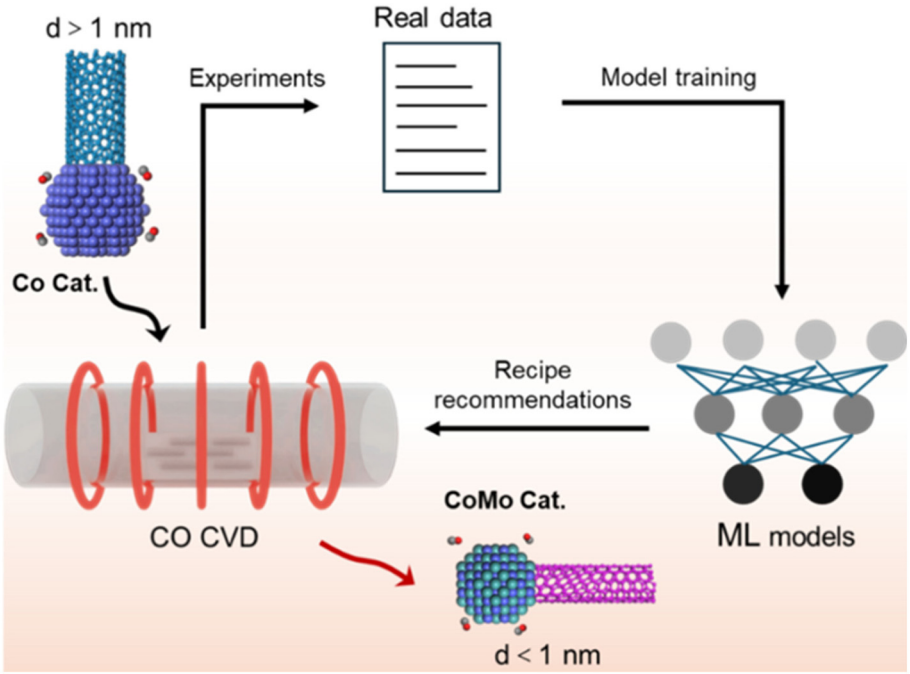

Fig. 1 Workflow for model development to guide the synthesis of a small-diameter SWNT horizontal array.

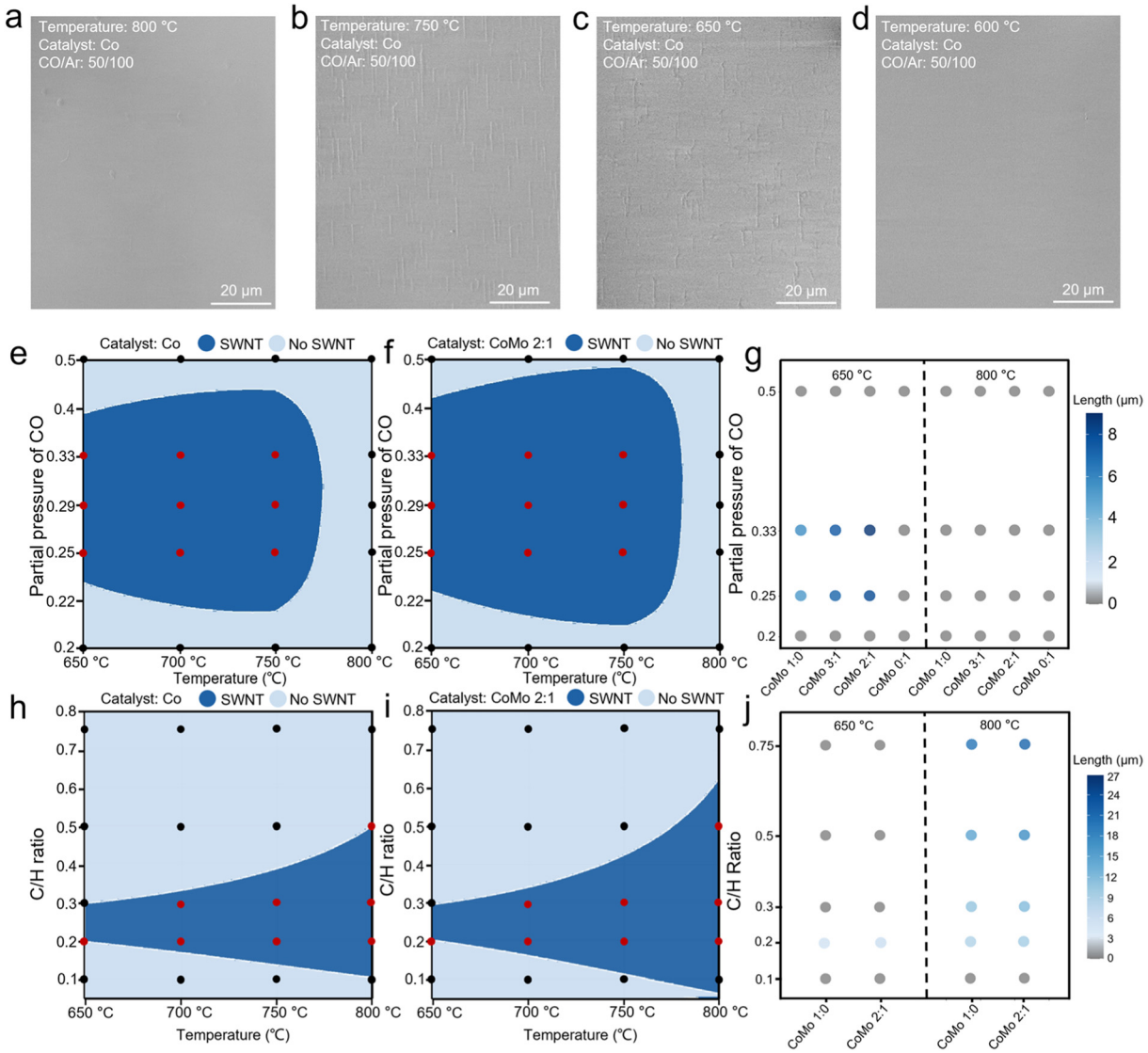

Fig. 2 Bayesian-model-guided analysis of SWNT growth windows and length statistics. (a–d) SEM images of quartz substrates loaded with Co catalysts after SWNT growth process under CO/Ar flow ratio of 50/100 at 800 °C, 750 °C, 650 °C, and 600 °C. (e and f) Growth windows of the Co (e) and Co/Mo (2 : 1) (f) catalysts obtained by classifying and predicting SWNT growth regions using a Bayesian model under varying temperatures and CO partial pressures (p_{CO}). (g) Average length statistics of SWNT arrays grown at 650 °C and 800 °C under orthogonal conditions defined by the Co/Mo ratio and p_{CO}. Dot with different colors represents the specific average length value. (h and i) Growth windows of Co (h) and Co/Mo (2 : 1) (i) catalysts obtained by Bayesian-model classification and prediction under varying temperatures and C/H ratios by using ethanol as the carbon source. (j) Average length statistics of SWNT arrays grown using ethanol at 650 °C and 800 °C under orthogonal conditions defined by the Co/Mo ratio and C/H ratio. Dot with different colors represents the specific average length value.

and controlling the synthesis of SWNTs. However, direct experimental mapping of this multi-parameter growth landscape is prohibitively labor-intensive and experimentally inefficient.

To overcome this limitation, we introduce an ML-assisted framework that enables the rapid and quantitative construction of SWNT growth windows from limited experimental data. A structured dataset was generated using an orthogonal experimental design that systematically varied the growth temperature and carbon-source concentration while minimizing experimental redundancy. All samples were characterized by scanning electron microscopy (SEM) (Fig. S1–S4), and the average nanotube length was extracted as a quantitative descriptor of growth behavior (Fig. S5–S7). For each catalyst system, 16 sets of orthogonal experiments were performed, yielding a compact but information-rich database suitable for ML analysis.

Then, a Bayesian logistic regression model was applied to probabilistically classify the growth and non-growth regimes while minimizing uncertainty in the growth boundaries. This model was selected for its robustness in small-sample, high-dimensional parameter spaces, as well as its ability to provide interpretable posterior distributions rather than deterministic predictions. The trained model exhibited excellent conver-

gence, with potential scale reduction factor ($\hat{E}$) values below 1.05 for all variables, including catalyst composition, CO partial pressure, and temperature, and sufficiently large effective sample sizes (ESS) for all posterior distributions (Fig. S8a and b). These diagnostics confirm the statistical reliability of the ML-derived growth windows. Detailed descriptions of the ML methodology, including model construction and validation procedures, are provided in the Methods section.

Using Co and Co/Mo (2 : 1) catalysts as representative examples (Fig. 2e and f, respectively), the ML model reveals well-defined decision boundaries separating growth and non-growth regions. Both catalysts exhibit relatively broad growth windows when CO is used as the carbon source. Notably, SWNT growth is consistently suppressed at temperatures above ~780 °C, whereas within the accessible growth regime, the dependence on temperature is comparatively weak. Comparative analysis across catalyst compositions, CO concentrations, and temperatures reveals a unified physical picture: catalytically active Co sites capable of dissociating CO are essential for enabling low-temperature SWNT growth, whereas excessively high temperatures universally suppress nanotube formation regardless of catalyst composition. This behavior reflects the thermodynamic and kinetic characteristics of CO cracking, in which elevated temperatures inhibit effective carbon incorporation into growing nanotubes. Correlation analysis of the full experimental-ML database further supports these conclusions (Fig. 2g and Fig. S8c). Together, these results demonstrate that low-temperature growth of horizontally aligned SWNT arrays can be efficiently achieved in a CO environment through the utilization of active Co sites.

However, the intrinsic role of temperature in SWNT growth cannot be fully resolved using CO as the sole carbon source, because CO cracking exhibits relatively weak temperature sensitivity within the growth window. To decouple temperature effects from carbon chemistry, additional carbon sources with distinct activation energies and decomposition pathways were introduced. Ethanol, a widely used carbon source for horizontally aligned SWNT arrays, was selected as a contrasting system. Accordingly, 16 sets of orthogonal experiments were conducted for both Co and Co/Mo (2 : 1) catalysts (Fig. S9 and S10, respectively) and analyzed using the same ML-assisted framework. As shown in Fig. 2h and i, the ethanol-based growth system exhibits growth windows that differ markedly from those observed for CO. In particular, the growth window narrows sharply with decreasing temperature, while increasing temperature significantly broadens the growth regime. This behavior reveals a strong and direct temperature dependence of SWNT growth in the ethanol system. Furthermore, pure Mo catalysts can serve as templates for SWNT growth at high temperatures when ethanol is used, but growth is entirely suppressed at low temperatures (Fig. 2j). These observations indicate that ethanol decomposition proceeds through two parallel pathways: thermal cracking and catalytic cracking. At high temperatures, ethanol can thermally decompose without catalytically active sites, generating sufficient carbon species for nanotube growth. In contrast, low-temperature growth relies predominantly on catalytic cracking, consistent with previous studies. Because ethanol has a relatively low activation energy for decomposition, catalytic cracking at low temperatures can generate excessive carbon species. Consequently, a high hydrogen concentration is required to suppress amorphous carbon accumulation and maintain the cleanliness of the catalyst surface. This requirement explains both the pronounced temperature sensitivity and the narrow growth windows observed in ethanol-based systems. Correlation analysis derived from the Bayesian ML model further substantiates these conclusions (Fig. S11). Collectively, these results establish ML-assisted growth-window construction as a powerful and generalizable strategy for decoding complex nanotube growth landscapes and for distinguishing the roles of carbon chemistry and temperature.

Based on the comparative analysis of the CO- and ethanol-based growth systems, we propose a microscopic mechanism governing the growth of horizontally aligned SWNT arrays at low temperatures (<800 °C). Three fundamental processes are involved: carbon atom generation, amorphous carbon accumulation, and SWNT growth. Carbon generation drives the latter two processes, which are intrinsically competitive. At low temperatures, amorphous carbon formation exhibits faster kinetics due to its lower activation barrier compared with SWNT nucleation. As illustrated in Fig. 3a, when the rate of carbon production (R_C) *via* catalytic cracking exceeds the rate of amorphous carbon formation (R_{AC}), rapid accumulation of amorphous carbon occurs on the catalyst surface, ultimately suppressing SWNT growth (Fig. 3b and c). Conversely, when R_C is lower than R_{AC} but higher than the SWNT growth rate (R_{GC}), corresponding to a graphitization-dominated regime, SWNT growth is favored (Fig. 3d and e). Thus, low-temperature SWNT growth emerges from a delicate balance among these three competing processes. This framework explains why ethanol-based growth requires high hydrogen concentrations at low temperatures, leading to window confinement, whereas the CO-based system readily enables low-temperature growth with a comparatively broad window.

Having established growth windows for low-temperature SWNT synthesis, we next investigated structural control within these windows. Selective SWNT growth arises from the combined effects of thermodynamic nucleation and kinetic growth on catalyst surfaces. Given the narrow growth window of ethanol, which disfavors thermodynamically prioritized selectivity, subsequent investigations were confined to the CO-based system. Key factors influencing thermodynamic selectivity, including catalyst composition, CO partial pressure, and growth temperature, were systematically explored through structural characterization of as-grown SWNT arrays. SWNT growth was carried out under varying temperatures and CO partial pressures using catalysts of different compositions, and the resulting horizontal arrays were characterized by Raman spectroscopy. As shown in Fig. 4a–f and Fig. S12–S14, increasing the Mo content in the catalyst led to a pronounced narrowing of the radial breathing mode (RBM) peak distribution,

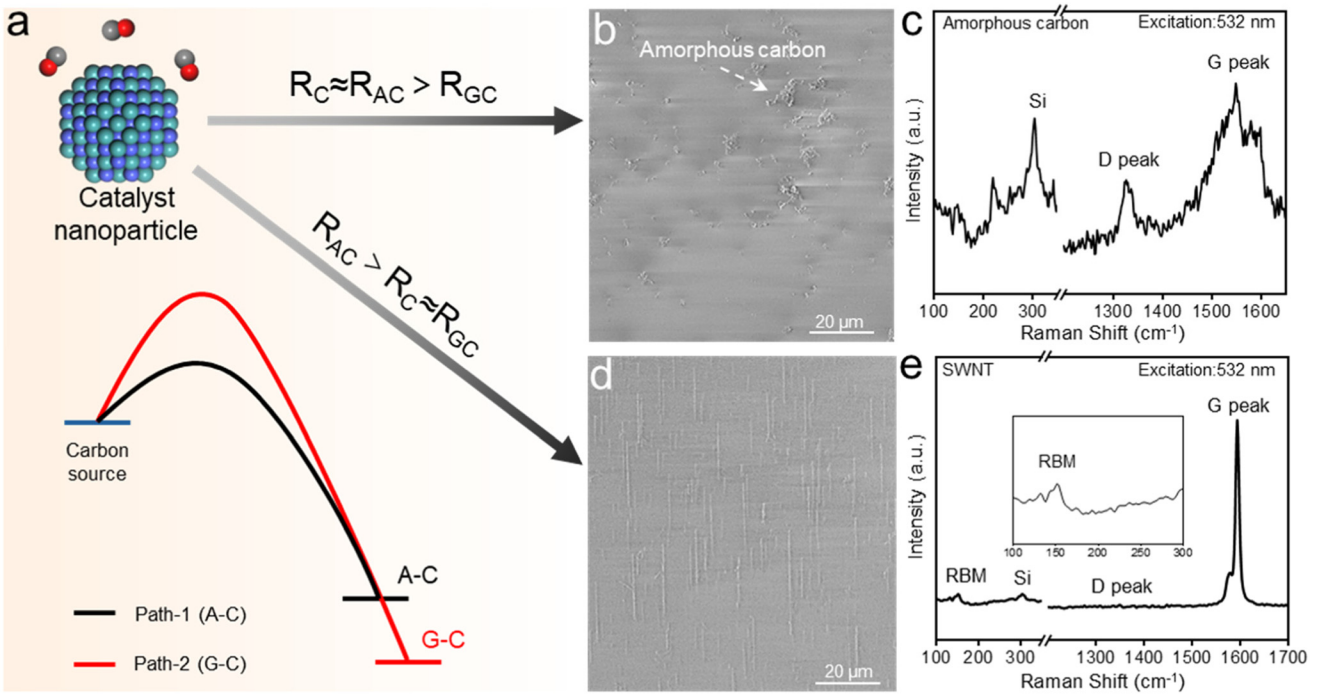

Fig. 3 (a) Illustration of two different reaction pathways of carbon source cracking on the CoMo catalyst at low temperatures: $R_C \approx R_{AC} > R_{GC}$ and $R_{AC} > R_C \approx R_{GC}$. (b and c) SEM image (b) and the corresponding Raman spectra (c) of the $R_C \approx R_{AC} > R_{GC}$ pathway. (d and e) SEM image (d) and the corresponding Raman spectra (e) of the $R_{AC} > R_C \approx R_{GC}$ pathway. The insert in (e) is an enlarged Raman spectrum between 100–300 cm^{-1} to show the existence of RNM peak.

whereas modest variations in CO partial pressure produced only minor changes within a given catalyst system. To quantify diameter selectivity, the RBM peak at 220 cm^{-1}, corresponding to SWNTs with a diameter of ~1 nm, was used as a threshold to distinguish small- (<1 nm) and large-diameter (>1 nm) nanotubes. Statistical analysis (Fig. 4g) reveals that for the pure Co catalyst, the fraction of small-diameter SWNTs decreases significantly with increasing temperature, likely due to catalyst coarsening induced by enhanced migration at elevated temperatures. In contrast, for the Co/Mo (2 : 1) catalyst under a CO/Ar flow ratio of 50 : 100, the relative abundance of small-diameter SWNTs increases from 50.0% to 84.6% as the temperature decreases. Across all the catalyst systems, the diameter selectivity exhibits weak dependence on the CO partial pressure, consistent with the intrinsically broad growth window of CO-based growth systems. These observations suggest that CO cracking proceeds relatively slowly, facilitating the interface-controlled, thermodynamically preferred growth of small-diameter SWNTs. The enhanced small-diameter selectivity observed for the Mo-rich catalysts at low temperatures, particularly at 650 °C, is attributed to the improved catalyst dispersibility and thermal stability of the catalyst structure arising from the high melting point of Mo.

To further quantify the relationships between growth parameters and structural selectivity, the relative abundances of different diameter populations were used as input variables for a Bayesian nonlinear ML model (Fig. 4h). The trained model also demonstrates good predictive accuracy, as confirmed by validation against experimental datasets (Fig. S15). Importantly, the model reveals a clear negative correlation between growth temperature and the abundance of small-diameter SWNTs, together with a positive correlation between small-diameter selectivity and molybdenum content in the catalyst. These statistical trends are fully consistent with the experimental observations and provide a quantitative framework for interpreting structure–growth relationships. Atomic force microscopy (AFM) analysis directly supports this interpretation, showing that catalysts with lower Co/Mo ratios exhibit more uniform nanoparticle dispersion and reduced average particle diameters (Fig. S16 and S17). These smaller and more stable nanoparticles provide energetically favorable nucleation sites for small-diameter SWNTs, thereby explaining the experimentally observed selective enrichment. Collectively, these results demonstrate that the catalyst composition governs the nanotube diameter not only through chemical activity but also by controlling the catalyst morphology and thermal stability during growth.

Guided by insights from the Bayesian nonlinear model, we propose a rational SWNT horizontal array strategy to further enhance the chiral selectivity at low temperatures. This strategy is based on three synergistic principles: minimizing the growth temperature to favor thermodynamic selectivity, maximizing the catalyst dispersion to suppress particle coarsening, and employing CO as a carbon source to provide a slow and controllable carbon flux. To experimentally validate this ML-guided strategy, the Mo content in the Co/Mo alloy catalyst was

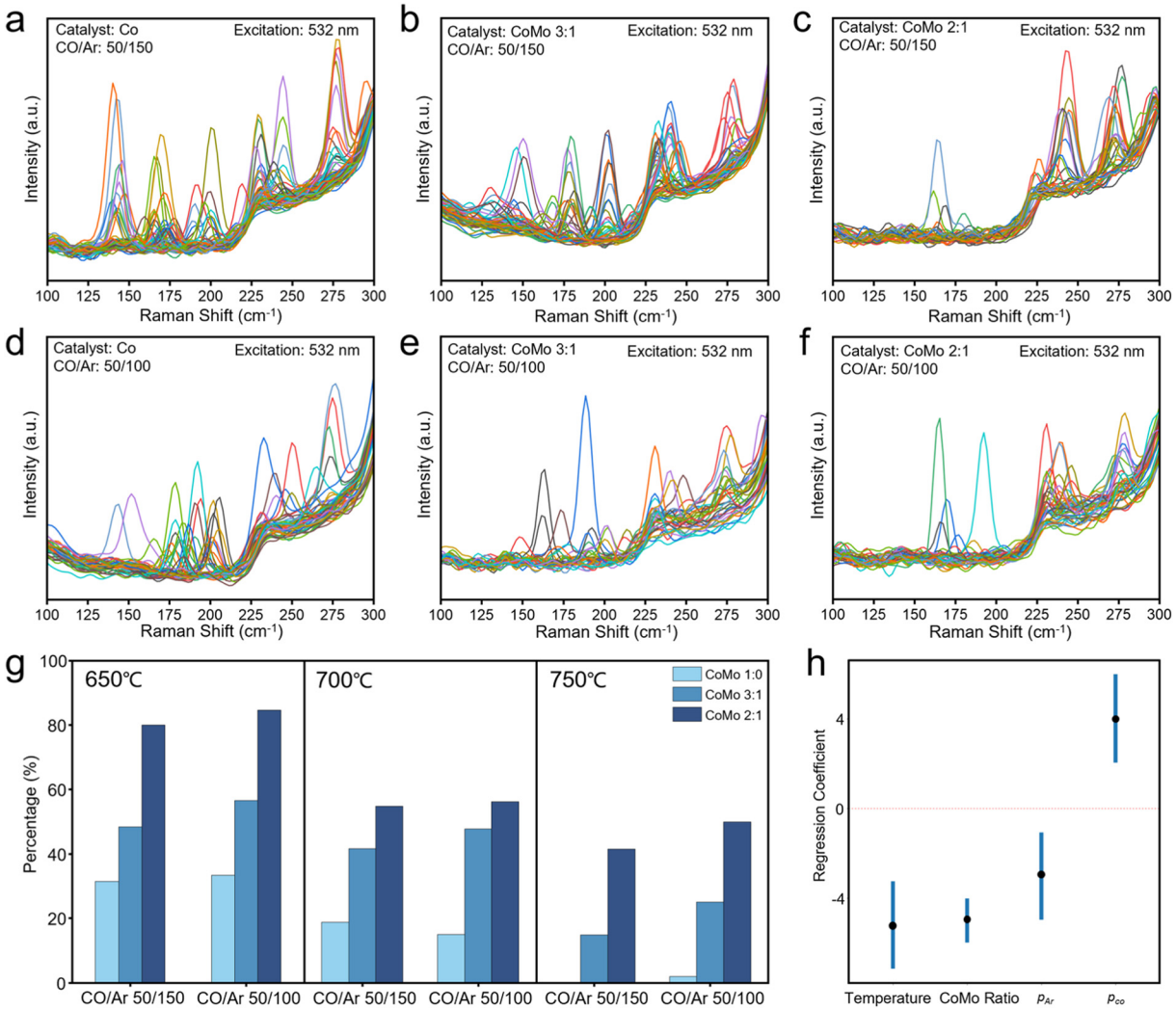

Fig. 4 (a–f) Raman spectra of SWNTs grown at 650 °C using three different CoMo ratio catalysts (Co/Mo 1 : 0; Co/Mo 3 : 1; and Co/Mo 2 : 1). Excitation wavelength: 532 nm. The carbon feeding conditions are indicated in each panel: CO/Ar 50/150 and 50/100. (g) Percentage of small-diameter SWNTs as a function of P_{CO}, catalyst ratio, and temperature. Three synthesis temperatures (650 °C, 700 °C, and 750 °C) are presented in separate subplots. Within each subplot, the horizontal axis denotes the CO/Ar flow ratio (50/100 and 50/150), and the fill color of the columns represents the CoMo catalyst ratio (1 : 0, 2 : 1, and 3 : 1). Column height indicates the percentage of small-diameter SWNTs determined by Raman spectral analysis. (h) Bayesian nonlinear regression posterior distribution of variables about small-diameter (diameter less than 1 nm or RBM peak larger than 220 cm^{-1}) selectivity.

further decreased to achieve a Co/Mo ratio of 1 : 1. The corresponding AFM characterization reveals a pronounced enhancement in catalyst dispersity, accompanied by a further reduction in the average particle diameter to 1.05 nm at 650 °C (Fig. S18). This behavior is attributed to the high melting point of Mo, which suppresses catalyst migration and aggregation under thermal conditions, as supported by Fig. S19. Transmission electron microscopy (TEM) analysis further confirms the formation of a homogeneous alloy structure (Co_2Mo_3) (Fig. S20 and 21), indicating intimate mixing of Co and Mo at the nanoscale.[36] These alloyed nanoparticles combine the catalytic activity of Co with the structural stabilization provided by Mo, yielding a catalyst architecture well suited for selective SWNT nucleation.

Using this optimized Co/Mo (1 : 1) catalyst, horizontally aligned SWNT arrays were grown on quartz substrates under CO at 650 °C, corresponding to the optimal growth window predicted by the Bayesian logistic regression model (Fig. S22). As shown in Fig. 5a, well-aligned SWNT horizontal arrays were obtained, with a linear density of approximately 1 tube per μm and a high degree of alignment along the substrate direction. Statistical analysis of the nanotube lengths indicates an average length of 9.87 μm, as displayed in Fig. 5b, demonstrating that enhanced selectivity is achieved without sacrificing growth efficiency. Raman spectroscopy measurements reveal pronounced enrichment of (6, 5) SWNTs, manifested as a dominant radial breathing mode (RBM) peak near 270 cm^{-1} (Fig. 5c). Systematic variation of the CO partial pressure shows

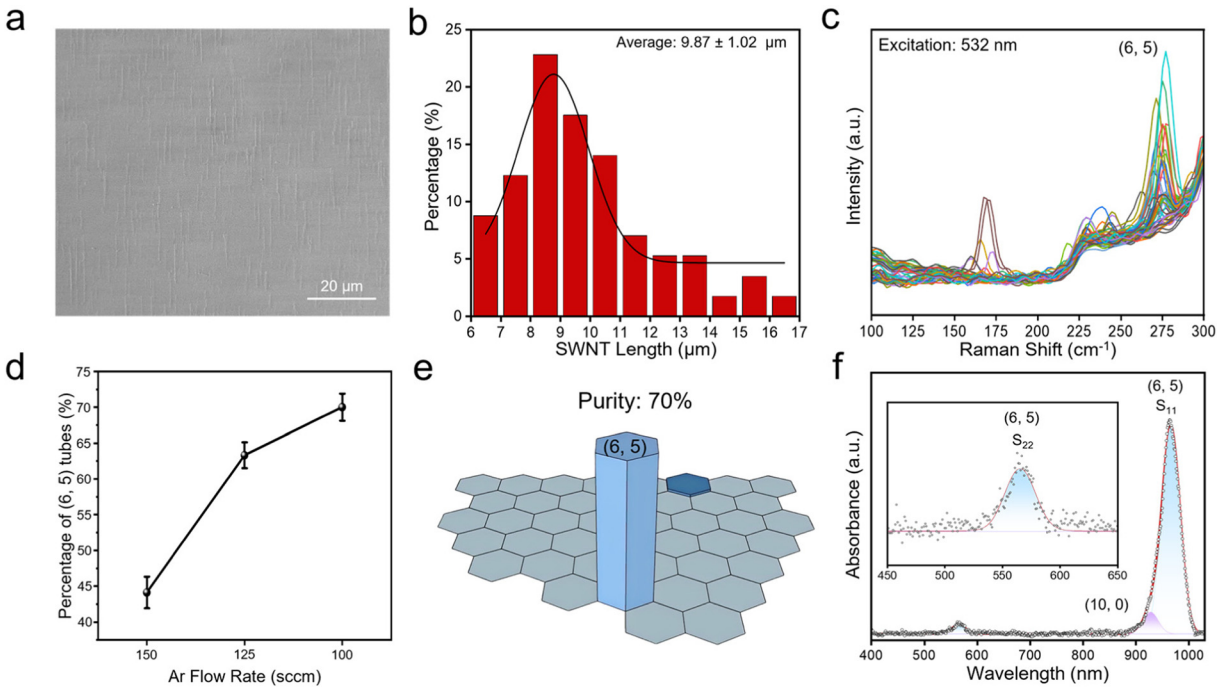

Fig. 5 Parameter optimization for the low-temperature growth of chiral SWNTs. (a) SEM image of SWNT horizontal array grown using a CoMo catalyst with a ratio of 1 : 1 under a CO/Ar flow ratio of 50/100 at 650 °C. (b and c) Corresponding length distribution (b) and Raman spectra (c) of the SWNT horizontal array in (a). (d) Abundance of (6, 5) tubes in the SWNT arrays grown with a Co–Mo catalyst ratio of 1 : 1 at 650 °C under different CO/Ar flow ratios. The flow rate of CO is maintained at 50 sccm. (e and f) (6, 5) tube relative abundance (e) and ultraviolet-visible-near-infrared absorption spectra (f) of SWNT array in (a).

that increasing the carbon flux further enhances the (6, 5) selectivity, reflecting the superior interfacial stability of this chirality with this Co/Mo (1 : 1) alloy catalyst (Fig. 5d). However, when the CO partial pressure approaches the upper boundary of the ML-predicted growth window, both alignment and areal density deteriorate, accompanied by the appearance of amorphous carbon. This behavior underscores the critical role of growth-window confinement in balancing the carbon supply, catalyst surface cleanliness, and selective nanotube nucleation. Ultimately, a maximum (6, 5) selectivity of 70% and an overall small-diameter selectivity of 91.2% were achieved (Fig. 5e), highlighting the effectiveness of the ML-guided growth strategy.

Additional spectroscopic characterization provides independent confirmation of the high chirality purity obtained under the optimized conditions. For example, the ultraviolet-visible-near-infrared absorption spectra (Fig. 5f and Fig. S23) of SWNTs dispersed from the substrate into solution exhibit a pronounced S_{11} transition at 967 nm, a typical characteristic of (6, 5) nanotubes, with minimal contributions from other chiral species. Although a weak feature that may be assigned to (10, 0) nanotubes is discernible in the ensemble absorption spectrum, its markedly lower intensity, together with the absence of statistically significant RBM signals in spatially localized Raman line-scan measurements, consistently indicates that these species, if present, exist only as a negligible minority. This result corroborates the Raman analysis and confirms that the observed enrichment originates from intrinsic growth selectivity rather than post-growth separation effects.

4. Conclusion

In summary, we establish a closed-loop, ML-driven framework that integrates limited experimental data, predictive modeling and targeted validation to resolve the multi-parameter landscape of SWNT growth systems. By quantitatively linking catalyst composition, growth conditions, and structural outcomes, this approach enables the rationally controlled synthesis of chirality-selective SWNTs at low temperatures. Guided by the predicted growth window, a Co/Mo (1 : 1) alloy catalyst was chosen at 650 °C to yield horizontally aligned SWNT arrays enriched in the thermodynamically dominant (6, 5) chirality with 70% selectivity for the first time. More broadly, the ML-assisted growth-window paradigm introduced here offers a general strategy for understanding and controlling complex material growth landscapes in low-dimensional nanomaterials.

Author contributions

Shuchen Zhang designed the experiments. Junxiao Li and Sizhe Lin performed the experiments and analyzed the results. Junxiao Li, Sizhe Lin, Wei Liu, Changlong Li, Jiacheng Song

and Zhiwei Liu performed the characterization measurement. Sizhe Lin, Junxiao Li, Yue Hu and Shuchen Zhang contributed to the writing and discussion of the manuscript.

Conflicts of interest

The authors declare no conflicts of interest.

Data availability

All data that support the findings of this study are included within the article and supplementary information (SI). Supplementary information is available, including SEM images of SWNT grown under different environment, detailed statistics on length of SWNTs and size of catalysts, Raman and TEM characterizations. See DOI: https://doi.org/10.1039/d5nr05458c.

Acknowledgements

We gratefully acknowledge the financial support from the National Natural Science Foundation of China (22494641 and GG2060007011), the Fundamental Research Funds for the Central Universities (grant KY2060000246, KB2060140008 and WK2490000002) and the Beijing National Laboratory for Molecular Sciences (BNLMS202406).

References

1 T. Rueckes, K. Kim, E. Joselevich, G. Y. Tseng, C. L. Cheung and C. M. Lieber, *Science*, 2000, **289**, 94–97.
2 P. Avouris, *Acc. Chem. Res.*, 2002, **35**, 1026–1034.
3 Q. Cao, S. J. Han, J. Tersoff, A. D. Franklin, Y. Zhu, Z. Zhang, G. S. Tulevski, J. S. Tang and W. Haensch, *Science*, 2015, **350**, 68–72.
4 S. Han, X. L. Liu and C. W. Zhou, *J. Am. Chem. Soc.*, 2005, **127**, 5294–5295.
5 L. Ding, A. Tselev, J. Y. Wang, D. N. Yuan, H. B. Chu, T. P. McNicholas, Y. Li and J. Liu, *Nano Lett.*, 2009, **9**, 800–805.
6 B. M. Everhart, R. Rao, P. Nikolaev, T. W. Liu, D. A. Gómez-Gualdrón, B. Maruyama and P. B. Amama, *Chem. Mater.*, 2022, **34**, 4548–4559.
7 B. Wang, C. H. P. Poa, W. Li, L. J. Li, Y. H. Yang and Y. Chen, *J. Am. Chem. Soc.*, 2007, **129**, 9014–9019.
8 T. R. Wang, J. Y. Hu, R. H. Ouyang, Y. T. Wang, Y. Huang, S. L. Hu and W. X. Li, *Science*, 2024, **386**, 915–920.
9 T. W. Hansen, A. T. DeLaRiva, S. R. Challa and A. K. Datye, *Acc. Chem. Res.*, 2013, **46**, 1720–1730.
10 M. S. He, Y. Magnin, H. Jiang, H. Amara, E. I. Kauppinen, A. Loiseau and C. Bichara, *Nanoscale*, 2018, **10**, 6744–6750.
11 S. Z. Lin, T. Ye, X. Y. Zhang, H. Zuo, L. X. Zhu, X. X. Wang, C. L. Li, Z. Yang, R. Du, D. W. Lin and Y. Hu, *Nano Today*, 2025, **61**, 102562.
12 M. Fouquet, B. C. Bayer, S. Esconjauregui, R. Blume, J. H. Warner, S. Hofmann, R. Schlögl, C. Thomsen and J. Robertson, *Phys. Rev. B:Condens. Matter Mater. Phys.*, 2012, **85**, 235411.
13 M. S. He, S. C. Zhang, Q. R. Wu, H. Xue, B. W. Xin, D. Wang and J. Zhang, *Adv. Mater.*, 2019, **31**, 1800805.
14 F. Yang, H. F. Zhao, R. M. Li, Q. D. Liu, X. R. Zhang, X. D. Bai, R. M. Wang and Y. Li, *Sci. Adv.*, 2022, **8**, eabq0794.
15 M. S. He, S. C. Zhang and J. Zhang, *Chem. Rev.*, 2020, **120**, 12592–12684.
16 M. S. He, H. Jiang, E. I. Kauppinen and J. Lehtonen, *Nanoscale*, 2012, **4**, 7394–7398.
17 M. S. He, X. Wang, S. C. Zhang, H. Jiang, F. Cavalca, H. Z. Cui, J. B. Wagner, T. W. Hansen, E. Kauppinen, J. Zhang and F. Ding, *Sci. Adv.*, 2019, **5**, eaav9668.
18 S. C. Zhang, X. Wang, F. R. Yao, M. S. He, D. W. Lin, H. Ma, Y. Y. Sun, Q. C. Zhao, K. H. Liu, F. Ding and J. Zhang, *Chem*, 2019, **5**, 1182–1193.
19 S. C. Zhang, L. X. Kang, X. Wang, L. M. Tong, L. W. Yang, Z. Q. Wang, K. Qi, S. B. Deng, Q. W. Li, X. D. Bai, F. Ding and J. Zhang, *Nature*, 2017, **543**, 234–238.
20 F. Yang, X. Wang, D. Q. Zhang, J. Yang, D. Luo, Z. W. Xu, J. K. Wei, J. Q. Wang, Z. Xu, F. Peng, X. M. Li, R. M. Li, Y. L. Li, M. H. Li, X. D. Bai, F. Ding and Y. Li, *Nature*, 2014, **510**, 522–524.
21 S. C. Zhang, D. W. Lin, W. M. Liu, Y. Yu and J. Zhang, *Small*, 2019, **15**, 1903896.
22 F. Q. Han, L. Qian, Q. R. Wu, D. Li, S. L. Hao, L. H. Feng, L. T. Xin, T. Yang, J. Zhang and M. S. He, *Carbon N. Y.*, 2022, **191**, 146–152.
23 G. Lolli, L. Zhang, L. Balzano, N. Sakulchaicharoen, Y. Q. Tan and D. E. Resasco, *J. Phys. Chem. B*, 2006, **110**, 2108–2115.
24 X. L. Li, X. M. Tu, S. Zaric, K. Welsher, W. S. Seo, W. Zhao and H. J. Dai, *J. Am. Chem. Soc.*, 2007, **129**, 15770–15771.
25 M. S. He, D. Li, T. Yang, D. H. Shang, A. I. Chernov, P. V. Fedotov, E. D. Obraztsova, Q. Liu, H. Jiang and E. Kauppinen, *Carbon N. Y.*, 2019, **153**, 389–395.
26 Y. Xu, E. Dervishi, A. R. Biris and A. S. Biris, *Mater. Lett.*, 2011, **65**, 1878–1881.
27 S. M. Bachilo, L. Balzano, J. E. Herrera, F. Pompeo, D. E. Resasco and R. B. Weisman, *J. Am. Chem. Soc.*, 2003, **125**, 11186–11187.
28 S. D. Liu, N. Cui, Q. R. Wu, K. Zhang, P. F. Wang, L. L. Dong and M. S. He, *Carbon N. Y.*, 2022, **191**, 433–438.
29 B. Wang, L. Wei, L. Yao, L. J. Li, Y. H. Yang and Y. Chen, *J. Phys. Chem. C*, 2007, **111**, 14612–14616.
30 H. Wang, L. Wei, F. Ren, Q. Wang, L. D. Pfefferle, G. L. Haller and Y. Chen, *ACS Nano*, 2013, **7**, 614–626.
31 Y. Hu, L. X. Kang, Q. C. Zhao, H. Zhong, S. C. Zhang, L. W. Yang, Z. Q. Wang, J. J. Lin, Q. W. Li, Z. Y. Zhang, L. M. Peng, Z. F. Liu and J. Zhang, *Nat. Commun.*, 2015, **6**, 6099.

32 E. Mjolsness and D. DeCoste, *Science*, 2001, **293**, 2051–2055.
33 R. Ramprasad, R. Batra, G. Pilania, A. Mannodi-Kanakkithodi and C. Kim, *npj Comput. Mater.*, 2017, **3**, 54.
34 G. H. Chen and D. M. Tang, *Nanomaterials*, 2024, **14**, 1688.
35 Y. Li, S. R. Wang, Z. Lv, Z. J. Wang, Y. B. Zhao, Y. Xie, Y. Xu, L. Qian, Y. D. Yang, Z. Q. Zhao and J. Zhang, *Matter*, 2025, **8**, 1.
36 L. Ni, K. Kuroda, L. P. Zhou, T. Kizuka, K. Ohta, K. Matsuishi and J. Nakamura, *Carbon N. Y.*, 2006, **44**, 2265–2272.